JM PAPERS

Stability analysis of time-periodic shear flow generated by an oscillating density interface

Lima Biswas[1] (iD) **and Anirban Guha**[2] (iD)

[1]Department of Mathematics, Gandhi Institute of Technology and Management (GITAM), Hyderabad 502329, India

[2]School of Science and Engineering, University of Dundee, Dundee DD1 4HN, UK

Corresponding author: Anirban Guha, anirbanguha.ubc@gmail.com

We consider the conceptual two-layered oscillating tank of Inoue & Smyth (2009 *J. Phys. Oceanogr.* vol. 39, no. 5, pp. 1150–1166), which mimics the time-periodic parallel shear flow generated by low-frequency (e.g. semi-diurnal tides) and small-angle oscillations of the density interface. Such self-induced shear of an oscillating pycnocline may provide an alternate pathway to pycnocline turbulence and diapycnal mixing in addition to the turbulence and mixing driven by wind-induced shear of the surface mixed layer. We theoretically investigate shear instabilities arising in the inviscid two-layered oscillating tank configuration and show that the equation governing the evolution of linear perturbations on the density interface is a Schrödinger-type ordinary differential equation with a periodic potential. The necessary and sufficient stability condition is governed by a non-dimensional parameter β resembling the inverse Richardson number; for two layers of equal thickness, instability arises when $\beta > 1/4$. When this condition is satisfied, the flow is initially stable but finally tunnels into the unstable region after reaching the time marking the turning point. Once unstable, perturbations grow exponentially and reveal characteristics of Kelvin–Helmholtz (KH) instability. The modified Airy function method, which is an improved variant of the Wentzel–Kramers–Brillouin theory, is implemented to obtain a uniformly valid, composite approximate solution to the interface evolution. Next, we analyse the fully nonlinear stages of interface evolution by modifying the circulation evolution equation in the standard vortex blob method, which reveals that the interface rolls up into KH billows. Finally, we undertake real case studies of Lake Geneva and Chesapeake Bay to provide a physical perspective.

Key words: internal waves, stratified flows, shear-flow instability

Figure 1. Schematic diagram of a two-layered oscillating tank, which can render short interfacial gravity waves unstable.

is the cornerstone of our analysis (although we also analyse the initial nonlinear stages of billow formation until saturation). As highlighted in Lewin & Caulfield (2022), the time of saturation of the KH billow relative to the time period of the background shear plays a central role in shaping the fully nonlinear stages of turbulent breakdown of the billow and therefore crucially affects the energetics and mixing. Since the standard linear stability analysis of stratified shear flows (Drazin & Reid 2004) is based on steady background conditions, it is unlikely to capture some of the key properties of instabilities arising in background flows with periodic time dependence. This necessitates a linear stability analysis of non-autonomous systems. Another key feature of this problem is the large separation of time scales – high-frequency interfacial waves (which are rendered unstable) being forced by low-frequency density interface oscillations. The numerical simulations of Inoue & Smyth (2009) and Lewin & Caulfield (2022) do not indicate any finely tuned frequency ratios for which the instability occurs. This implies that parametric instability, for example, the problem studied in Kelly (1965), is unlikely to be the driving mechanism. Along similar lines, the generalised stability theory for non-autonomous systems (Farrell & Ioannou 1996) might not be best suited for the purpose of this study. This necessitates a bespoke analysis starting from the fundamental principles.

The paper is organised as follows. Section 2 discusses the governing equations for the background flow and adds linear perturbations to the system to derive the equation governing the interfacial dynamics. The condition for instability is also obtained. Section 3 deals with various kinds of linear stability analyses, e.g. Floquet theory, normal-mode theory (based on steady-state analysis) and the modified Airy function (MAF) technique, and provides comparisons with numerical solutions. Building on the current vortex method technique, § 4 incorporates unsteady effects and captures the nonlinear evolution of the interface. Physical interpretation of the system is provided in § 5 by undertaking two case studies – Lake Geneva and Chesapeake Bay. Finally, the paper is summarised and concluded in § 6.

2. Governing equations

2.1. *Background flow*

We consider the two-dimensional (2-D) flow produced by oscillating a horizontal tank having a rectangular cross-section of depth h, while the along-channel (x) and cross-channel (y) dimensions are infinite. The z direction is positive upward; see figure 1 for

the schematic of the set-up. The tank consists of a Boussinesq, two-layered, inviscid and immiscible fluid with the following density distribution:

$$\rho(z) = \begin{cases} \rho_1 & 0 < z < h/2, \\ \rho_2 & -h/2 < z < 0. \end{cases} \tag{2.1}$$

The fluid is stably stratified, i.e. $\rho_1 < \rho_2$. A more generic setting in which the two layers have unequal depths is discussed in Appendix A. Throughout the paper, subscripts 1 and 2 will respectively denote quantities associated with the upper and lower fluid layers. The system is restricted to a small angle of oscillation $\alpha(t)$, typically max $|\alpha(t)| \lesssim 7°$. The small tilt of the density interface functions as a geophysically plausible mechanism for generating shear; the vertical motions induced by the sloping interface have a negligible effect on the fluid dynamics (Lewin & Caulfield 2022). For the setting in figure 1, the governing Navier–Stokes equations under the Boussinesq approximation read (Inoue & Smyth 2009; Lewin & Caulfield 2022)

$$\frac{\mathrm{D}u}{\mathrm{D}t} = -\frac{1}{\rho_0}\frac{\partial p}{\partial x} - g\frac{\rho}{\rho_0}\sin\alpha(t) + 2\alpha_{,t}w, \tag{2.2a}$$

$$\frac{\mathrm{D}w}{\mathrm{D}t} = -\frac{1}{\rho_0}\frac{\partial p}{\partial z} - g\frac{\rho}{\rho_0}\cos\alpha(t) - 2\alpha_{,t}u. \tag{2.2b}$$

Here, $\mathrm{D}/\mathrm{D}t = \partial/\partial t + \boldsymbol{u}\cdot\boldsymbol{\nabla}$, where $\boldsymbol{\nabla} = (\hat{\boldsymbol{x}}\,\partial/\partial x,\ \hat{\boldsymbol{z}}\,\partial/\partial z)$, $\boldsymbol{u} = (u,\ w)$ is the velocity vector, ρ_0 is the constant reference density, g is the acceleration due to gravity and the suffix, '$_{,t}$' denotes ordinary derivative $\mathrm{d}/\mathrm{d}t$. The last terms in (2.2a)–(2.2b) represent Coriolis accelerations arising from the time-dependent rotation. The incompressibility condition is satisfied by the continuity equation

$$\frac{\partial u}{\partial x} + \frac{\partial w}{\partial z} = 0. \tag{2.3}$$

The background state velocity is assumed to be parallel to the x-axis, i.e. $\boldsymbol{U} = (U, 0)$. Hence, the continuity equation, (2.3), implies that U is only a function of z and t. Therefore, the background state equations yield

$$\frac{\partial U}{\partial t} = -\frac{1}{\rho_0}\frac{\partial P}{\partial x} - g\frac{\rho}{\rho_0}\sin\alpha(t), \tag{2.4a}$$

$$P = -\int \left[g\rho(z)\cos\alpha(t) + 2\rho_0\alpha_{,t}U(z,t)\right]\mathrm{d}z + \mathcal{G}(x,t), \tag{2.4b}$$

where $P(x, z, t)$ denotes the background state pressure.

Equation (2.1) indicates that ρ is a function of z only. Consequently from (2.4b), $P(x, z, t)$ can be expressed as the sum of a function that is dependent on z and t, and another function $\mathcal{G}$ dependent on x and t. This implies $\partial P/\partial x$ is a function of x and t. However, as per (2.4a), both $\partial U/\partial t$ and $g(\rho/\rho_0)\sin\alpha(t)$ are functions of z and t only. Therefore, $\partial P/\partial x$ must be a function of t alone. Since the tank is enclosed and there is no net flux across the walls, we must have (Thorpe 1969)

$$\int_{-h/2}^{h/2} U(z, t)\,\mathrm{d}z = 0. \tag{2.5}$$

The above condition can be used to obtain the background state velocity profile. In this regard, we integrate (2.4a) in both z and t and substitute (2.5)

$$\int_0^t \frac{\partial P}{\partial x}\mathrm{d}t = -\frac{g}{h}\int_{-h/2}^{h/2}\rho\,\mathrm{d}z\int_0^t \sin\alpha(\tilde{t})\,\mathrm{d}\tilde{t}. \tag{2.6}$$

Finally, we integrate (2.4*a*) in t and combine with (2.6) and (2.1), which yields the background state velocity profile

$$U(z, t) = \begin{cases} U_1(t) = \dfrac{g'}{2} \displaystyle\int_0^t \sin \alpha(\tilde{t}) \, \mathrm{d}\tilde{t} & 0 < z < h/2, \\[4mm] U_2(t) = -\dfrac{g'}{2} \displaystyle\int_0^t \sin \alpha(\tilde{t}) \, \mathrm{d}\tilde{t} & -h/2 < z < 0, \end{cases} \tag{2.7}$$

where $g' = g(\rho_2 - \rho_1)/\rho_0$ is the reduced gravity. We assume that the tilt angle varies sinusoidally with time

$$\alpha(t) = \alpha_f \sin(\omega_f t), \tag{2.8}$$

where α_f and ω_f respectively denote the maximum angular amplitude and frequency of oscillation of the tilted tank. Since we have restricted our study to small oscillations ($\alpha_f \ll 1$), this implies $\sin \alpha \approx \alpha$ and $\cos \alpha \approx 1 - \alpha^2/2$. Under this assumption, the background state velocity in (2.7) simplifies to

$$U_1(t) = \frac{g'}{2} \frac{\alpha_f}{\omega_f} [1 - \cos(\omega_f t)] \quad 0 < z < h/2, \tag{2.9a}$$

$$U_2(t) = -\frac{g'}{2} \frac{\alpha_f}{\omega_f} [1 - \cos(\omega_f t)] \quad -h/2 < z < 0. \tag{2.9b}$$

The fact that the signs in (2.9*a*)–(2.9*b*) agree with our intuition can be verified by simply inspecting figure 1, which can be regarded as the maximum angle in the counter-clockwise direction attained by the tank, equalling α_f. As per (2.8) this implies $\omega_f t = \pi/2$, which, when substituted into (2.9*a*)–(2.9*b*), yields $U_1 = -U_2 = g'\alpha_f/2\omega_f$. The signs make sense because the heavier, lower layer must have a negative velocity since it would flow downwards due to gravity, and the upper layer should compensate for this by flowing upwards, yielding a positive velocity.

2.2. *Linear perturbations*

We now consider the effect of infinitesimal perturbations added to the background state, and follow an approach similar to Thorpe (1969). The displacement of the two-fluid interface, given by $z = \xi(x, t)$, sets up an irrotational perturbation velocity field in the two layers. The total velocity reads

$$\boldsymbol{u} = \begin{cases} U_1(t)\hat{\boldsymbol{x}} + \nabla\phi_1(x, z, t) & 0 < z < h/2, \\ U_2(t)\hat{\boldsymbol{x}} + \nabla\phi_2(x, z, t) & -h/2 < z < 0, \end{cases} \tag{2.10}$$

where ϕ_1 and ϕ_2 are, respectively, the perturbation velocity potentials in the upper and lower fluid layers, which satisfy Laplace's equation in their respective layers

$$\nabla^2 \phi_1 = 0 \quad 0 < z < h/2, \tag{2.11a}$$

$$\nabla^2 \phi_2 = 0 \quad -h/2 < z < 0. \tag{2.11b}$$

The linearised dynamical boundary conditions at $z = 0$ for the two layers are as follows:

$$\frac{P_1}{\rho_1} + \frac{\partial\phi_1}{\partial t} + \frac{\partial}{\partial t}(U_1 x) + U_1 \frac{\partial\phi_1}{\partial x} + gx \sin \alpha(t) + gz \cos \alpha(t) = A_1(t), \tag{2.12a}$$

$$\frac{P_2}{\rho_2} + \frac{\partial\phi_2}{\partial t} + \frac{\partial}{\partial t}(U_2 x) + U_2 \frac{\partial\phi_2}{\partial x} + gx \sin \alpha(t) + gz \cos \alpha(t) = A_2(t), \tag{2.12b}$$

1015 A27-5

where P_1 and P_2, respectively, denote pressure in the upper and lower fluid layers, and A_1 and A_2 are arbitrary functions of time. Likewise, the linearised kinematic boundary conditions at $z = 0$ for the two layers read

$$\frac{\partial \xi}{\partial t} + U_1(t)\frac{\partial \xi}{\partial x} = \frac{\partial \phi_1}{\partial z}, \tag{2.13a}$$

$$\frac{\partial \xi}{\partial t} + U_2(t)\frac{\partial \xi}{\partial x} = \frac{\partial \phi_2}{\partial z}. \tag{2.13b}$$

The upper and lower boundaries satisfy the impermeability condition

$$\frac{\partial \phi_1}{\partial z} = 0 \quad \text{at} \quad z = h/2, \tag{2.14a}$$

$$\frac{\partial \phi_2}{\partial z} = 0 \quad \text{at} \quad z = -h/2. \tag{2.14b}$$

Next, we assume the perturbations in the form of Fourier modes

$$\xi(x, t) = \eta(t)e^{ikx}, \tag{2.15a}$$

$$\phi_1(x, z, t) = \psi_1(t)\cosh k\left(z - \frac{h}{2}\right)e^{ikx}, \tag{2.15b}$$

$$\phi_2(x, z, t) = \psi_2(t)\cosh k\left(z + \frac{h}{2}\right)e^{ikx}, \tag{2.15c}$$

where k denotes the wavenumber and it is understood that the real parts of terms appearing on the right-hand sides are to be taken. It is straightforward to verify that the perturbation velocity potentials satisfy Laplace's equations (2.11a)–(2.11b) and the impermeability condition (2.14a)–(2.14b). The continuity of pressure across the interface ($P_1 = P_2$) is applied in (2.12a)–(2.12b), thereby combining these two equations into one

$$\rho_1 A_1 - \rho_1 \psi_{1,t}\cosh\left(\frac{kh}{2}\right)e^{ikx} - \rho_1 x U_{1,t} - ik\rho_1 U_1\psi_1\cosh\left(\frac{kh}{2}\right)e^{ikx} - \rho_1 g x\sin\alpha(t)$$

$$- \rho_1 g\eta\cos\alpha(t)e^{ikx} = \rho_2 A_2 - \rho_2\psi_{2,t}\cosh\left(\frac{kh}{2}\right)e^{ikx} - \rho_2 x U_{2,t}$$

$$- ik\rho_2 U_2\psi_2\cosh\left(\frac{kh}{2}\right)e^{ikx} - \rho_2 g x\sin\alpha(t) - \rho_2 g\eta\cos\alpha(t)e^{ikx}. \tag{2.16}$$

Note that, in the above equation, we have substituted (2.15a)–(2.15c). Next we collect the coefficients of e^{ikx} (Thorpe 1969, Appendix A), and invoke the Boussinesq approximation

$$\left(\psi_{1,t} - \psi_{2,t}\right)\cosh\left(\frac{kh}{2}\right) + ik\left(U_1\psi_1 - U_2\psi_2\right)\cosh\left(\frac{kh}{2}\right) = g'\eta\cos\alpha(t). \tag{2.17}$$

Finally, we substitute the linearised kinematic boundary conditions (2.13a)–(2.13b) in the above equation, yielding a second-order ordinary differential equation (ODE) only in terms of η

$$\eta_{,tt} + \left[\underbrace{\frac{kg'}{2}\tanh\left(\frac{kh}{2}\right)}_{\omega^2}\cos\alpha(t) - \frac{k^2}{2}\left(U_1(t)^2 + U_2(t)^2\right)\right]\eta = 0. \tag{2.18}$$

The explicit time dependence of the background flow has been intentionally emphasised. For a tank at rest, meaning $\alpha = 0$ and $U_1 = U_2 = 0$, we recover the equation governing

interfacial gravity waves with frequency $\omega = \pm\sqrt{(g'k/2)\tanh(kh/2)}$ propagating in a two-layered fluid where each layer has a depth of $h/2$, see Sutherland (2010). Hereafter, we will restrict our attention to $\tanh(kh/2) \approx 1$, i.e. the waves are much shorter than the depth of the individual layers. The justification behind this choice is motivated by the fact that the wavelengths of KH instabilities arising in the pycnocline are usually much smaller than the pycnocline's depth. Hence, the layer depths do not play any further role in governing the dynamics.

Substituting (2.9a)–(2.9b) into (2.18) yields

$$\eta_{,tt} + \left[\omega^2\left(1 - \frac{\alpha_f^2}{4}(1 - \cos(2\omega_f t))\right) - \omega^4\frac{\alpha_f^2}{\omega_f^2}\left(\frac{3}{2} - 2\cos\left(\omega_f t\right) + \frac{1}{2}\cos\left(2\omega_f t\right)\right)\right]\eta = 0. \tag{2.19}$$

Hereafter, ω_f will represent low-frequency oscillations of the density interface. Physically, this can represent low-order, basin-scale modes (Sutherland 2010, Chapter 2.5) which are essentially standing waves equivalent to seiches in lakes. Furthermore, although the analogy is tenuous, ω_f can also represent the frequency of propagating long interfacial waves; see Inoue & Smyth (2009). In any case, the two-layered oscillating tank set-up in figure 1 is a simplified representation of the realistic scenario, and the key outcome in this context is the appearance of a small parameter $\epsilon = \omega_f/\omega \ll 1$. In other words, the frequencies (wavelengths) of the gravity waves at the density interface, which could be rendered unstable, are orders of magnitude greater (smaller) than the frequencies (wavelengths) characterising the mean density interface, i.e. the background flow. The mean density interface represents a small-amplitude long wave of infinite wavelength, which essentially makes it a straight line and further ensures that the background shear flow is parallel.

Defining a non-dimensional time $\tau = \omega_f t$, (2.19) yields

$$\epsilon^2\eta_{,\tau\tau} + \left[\underbrace{1 - \frac{3}{2}\beta + \beta\left(2\cos\left(\tau\right) - \frac{1}{2}\cos\left(2\tau\right)\right)}_{\mathcal{F}(\tau)} - \frac{\alpha_f^2}{4}(1 - \cos(2\tau))\right]\eta = 0, \tag{2.20}$$

where $\beta = \alpha_f^2/\epsilon^2$. Comparing β with the definition of minimum Richardson number Ri_{min} in Inoue & Smyth (2009), Equation (13), we observe that β resembles the inverse of minimum Richardson number. However, we are cautious that there is no length scale (shear layer thickness) in our problem, hence a direct comparison with Inoue & Smyth (2009) might be misleading. Note that $\beta \gg \alpha_f^2$, thus $\mathcal{O}(\alpha_f^2)$ terms can be neglected. This transforms (2.20) into the following governing equation of the interface, which can be classified as a Schrödinger-type equation with a periodic potential:

$$\epsilon^2\eta_{,\tau\tau} + \mathcal{F}(\tau)\eta = 0 \quad \text{where } \mathcal{F}(\tau) = \mathcal{F}(\tau + 2\pi). \tag{2.21}$$

It is worthwhile to compare (2.21) with the governing ODE obtained by Kelly (1965), Equation (3.17). Kelly's two-layered flow with imposed layer-wise oscillating shear is only applicable to non-Boussinesq flows (shear disappears under the Boussinesq limit, see Kelly 1965, Equation (2.3)) and hence is fundamentally different from our system. The ODE governing Kelly's system is Mathieu-type and therefore undergoes parametric instability when the forcing frequency ω_f is twice the natural frequency ω. Such parametric resonance is not expected to be the mechanism driving instability in our system since ω and ω_f differ by many orders of magnitude. Furthermore, previous authors (Inoue & Smyth 2009; Lewin & Caulfield 2022) do not report any finely tuned frequency

ratios for observing the instability. The order separation of the two frequencies gives rise to the coefficient ϵ^2 in the second derivative, thereby rendering (2.21) into a Schrödinger-type equation. We note in passing that Onuki, Joubaud & Dauxois (2021) numerically studied the situation for which $\omega \sim \omega_f$ (hence $\epsilon \sim 1$), and indeed the authors report parametric subharmonic instability.

2.2.1. *Necessary and sufficient condition for instability*

The nature of the solution to (2.21) is determined by the sign of $\mathcal{F}(\tau)$; instability implies $\mathcal{F}(\tau) < 0$ while the flow is stable for $\mathcal{F}(\tau) > 0$. After some algebra, the necessary and sufficient condition for instability is found to be

$$\cos \tau < 1 - \frac{1}{\sqrt{\beta}} \implies \beta > \beta_{min} = \frac{1}{4}. \qquad (2.22)$$

This implies all waves with wavenumbers $k > k_{long\text{-}wave\text{-}cut\text{-}off} = \omega_f^2 / 2g'\alpha_f^2$ are unstable. Figure 2 represents the variation of $\mathcal{F}(\tau)$ with τ for various β values. Initially, the flow is stable for all finite β values. For $\beta > 0.25$, the solution 'tunnels' into the unstable region after crossing the (first) turning point $\tau = \tau_c$, which signifies $\mathcal{F}(\tau)$ changing sign from positive to negative. From (2.22), τ_c can be straightforwardly determined

$$\tau_c = \cos^{-1}\left(1 - \frac{1}{\sqrt{\beta}}\right). \qquad (2.23)$$

Noting that $\mathcal{F}(\tau)$ has a period of 2π and a mirror symmetry about $\tau = \pi$, it changes sign (for $\beta > 0.25$) twice within its period – first at $\tau = \tau_c$ and then at $\tau = 2\pi - \tau_c$. The stability condition provides an upper bound for the time of occurrence of the instability – if the flow is unstable, then instability will set in before $\tau = \pi$. The second turning point at $\tau = 2\pi - \tau_c$ signifies stabilisation, which may have little effect for higher β values that allow sustained growth for a longer time interval $(2\pi - 2\tau_c)$. This is because τ_c reduces as β increases. Hence, the role of β is analogous to that of the inverse of the Richardson number.

In Appendix A, we discuss the generic situation in which the two fluid layers have unequal depths: h_1 and $h_2 = h - h_1$. In this scenario, the necessary and sufficient condition for instability is given by (see (A5))

$$\beta > \beta_{min} = \frac{1}{8\left[r^2 + (1-r)^2\right]}, \qquad (2.24)$$

where $r = h_1/h$. Since $r \in (0, 1)$, we must have $1/8 < \beta_{min} \leqslant 1/4$. The upper bound for the time of occurrence of the instability is independent of r and occurs at $\tau = \pi$. In the oceanographic context, the typical depth of the pycnocline (h_1) is much less than the total ocean depth (h), i.e. $r \ll 1$, which leads to the instability condition $\beta > 1/8$.

2.2.2. *Predictions from the steady background flow assumption*

Undertaking a conventional, steady-state-based linear stability analysis for an inherently unsteady background flow could appear simplistic. However, such an analysis has a key advantage – the simplifications can result in an exact solution of (2.21), leading to a closed-form expression for the growth rate. Furthermore, if the growth is exponential (verified *a posteriori*), then the time scale of growth is much faster than the slow time dependence of the background flow, implying that the steady-state assumption is sensible. Here we intend to explore the predictions obtained from steady-state-based analyses and the extent of errors incurred.
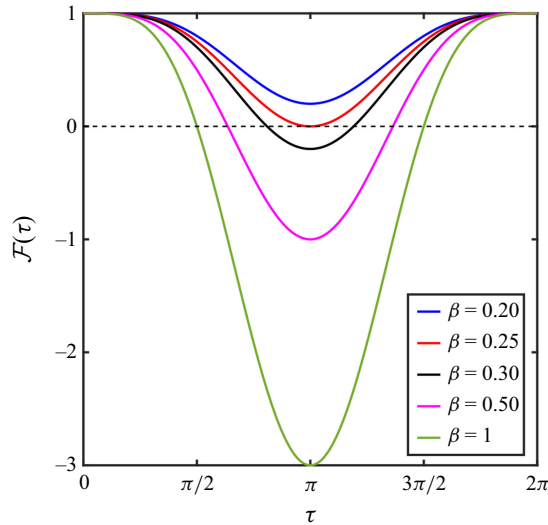
Figure 2. Variation of $\mathcal{F}(\tau)$ with τ for different β values. The flow becomes unstable when $\mathcal{F}(\tau) < 0$. For reference, $\tau = \pi/2$ implies the maximum counter-clockwise excursion (i.e. $\alpha = \alpha_f$) of the two-layered oscillating tank, while $\tau = \pi$ implies that the tank, through clockwise rotation, has reached the horizontal position.

One way of removing the explicit time dependence of the background flow is time averaging. By averaging (2.9a)–(2.9b) over its period, we obtain

$$\overline{U_1} = -\overline{U_2} = \frac{g'}{2} \frac{\alpha_f}{\omega_f}, \tag{2.25}$$

which when substituted into (2.18) converts (2.21) into a second-order constant coefficient ODE with $\mathcal{F} = 1 - \beta$. This yields the instability condition $\beta > 1$, which implies normal-mode instabilities with a growth rate of $\sigma_{normal\text{-}mode} = \sqrt{\beta - 1}/\epsilon$. Comparison with (2.22) shows that the above instability condition is erroneous.

Next, we undertake another steady-state-based approach where the maximum background velocity of each layer given in (2.9a)–(2.9b) is considered

$$U_{1,max} = -U_{2,max} = g' \frac{\alpha_f}{\omega_f}. \tag{2.26}$$

The above background velocities are substituted in (2.18) yielding $\mathcal{F} = 1 - 4\beta$ in the governing equation (2.21). This flow becomes unstable to normal-mode instabilities which has a growth rate of

$$\sigma_{normal\text{-}mode} = \frac{\sqrt{4\beta - 1}}{\epsilon}. \tag{2.27}$$

The resulting instability condition $\beta > 1/4$ exactly matches the unsteady analysis in (2.22). To see how this growth rate compares with the classical KH instability of two discontinuous layers, we write the well-known expression for its dimensional growth rate (Drazin & Reid 2004; Guha & Rahmani 2019)

$$\widetilde{\sigma}_{KH} = \sqrt{U^2 k^2 - \frac{g'k}{2}}, \tag{2.28}$$

L. Biswas and A. Guha

where the upper (lower) layer of density ρ_1 (ρ_2) is moving with a constant velocity U ($-U$). Substituting $U = U_{1,max}$ from (2.26) and non-dimensionalising (2.28) with ω_f, it is straightforward to verify that the non-dimensional growth rate $\sigma_{KH} = \tilde{\sigma}_{KH}/\omega_f = \sigma_{normal-mode}$ in (2.27).

In summary, the steady-state-based linear stability analysis that considers the maximum (instead of time-average) background velocity in each layer provides the same instability condition as the time-dependent problem. The normal-mode growth rate exactly matches the classical KH instability. However, such an analysis is unable to capture key features of the actual system, which is inherently unsteady. For example, the steady-state-based analysis cannot predict the time of onset of the instability. Since τ is a slow time, a delayed onset of instability is a salient feature of this system. How well the growth rate predicted from the steady-state-based analysis compares with the unsteady analysis also needs to be examined.

3. Linear stability analysis

3.1. *Floquet analysis, numerical integration and normal-mode predictions*

Equation (2.21) can be written as a 2-D dynamical system

$$\begin{bmatrix} \eta \\ v \end{bmatrix}_{,\tau} = \underbrace{\begin{bmatrix} 0 & 1 \\ -\epsilon^{-2}\mathcal{F}(\tau) & 0 \end{bmatrix}}_{\mathcal{L}(\tau)} \begin{bmatrix} \eta \\ v \end{bmatrix}, \tag{3.1}$$

where the linear operator $\mathcal{L}(\tau)$ has a fundamental period of $T = 2\pi$. The fundamental solution matrix $\Phi(\tau)$ satisfies

$$\Phi_{,\tau}(\tau) = \mathcal{L}(\tau)\Phi(\tau) \quad \text{where} \quad \Phi(0) = I. \tag{3.2}$$

Floquet analysis is the standard technique for analysing the stability of linear periodic systems. If the analysis finds that the energy of the disturbance at the end of one period is larger than the energy at the outset, the system is deemed unstable. In this regard, the monodromy matrix $\Phi(T)$ (which is numerically computed in general) is first determined and its eigenvalues, known as Floquet multipliers μ, are sought. The Floquet exponents Ω, signifying the complex temporal growth rate, are related to the Floquet multipliers via the relation $\mu = \exp(\Omega T)$. The system is deemed unstable if there exists at least one eigenvalue satisfying $|\mu| > 1$ ($\mathrm{Re}(\Omega) > 0$). Likewise, the system is stable if all eigenvalues satisfy $|\mu| < 1$ ($\mathrm{Re}(\Omega) < 0$). When all eigenvalues satisfy $|\mu| = 1$ ($\mathrm{Re}(\Omega) = 0$), the system oscillates between finite bounds $\forall \tau$ (Richards 2002). In this case, the solution is neutrally stable and can yield quasiperiodic behaviour in time (Kovacic, Rand & Mohamed Sah 2018).

We compute Floquet exponents and the Floquet multipliers using Matlab corresponding to different β values in table 1. We keep α_f fixed at 0.05 (which is equivalent to 2.86°) in the entire paper. The system is bounded for $\beta = 0.1$ and 0.2, and unstable for 0.27, 0.3 and 0.35, which are the expected outcomes as per the condition in (2.22). Furthermore, we also observe that, when $\beta > 0.25$, the higher the β value, the higher the maximum growth rate $\mathrm{Re}(\Omega_{max})$. We restrict our Floquet analysis to up to $\beta = 0.35$ since, beyond this value, the numerical solution becomes unreliable owing to the resulting extremely large and extremely small Floquet multipliers.

To understand how the amplitude evolves in time, and to explore a bigger range of β values, we numerically solve (2.21) using Matlab's inbuilt ODE45 solver (which was also used to construct the monodromy matrix while performing the Floquet analysis). For the two initial conditions, we take

1015 A27-10

β	μ_1	μ_2	$|\mu_{max}|$	$\mathrm{Re}(\Omega_{max})$
0.1	0.3564 − 0.9343i	0.3564 + 0.9343i	1	0
0.2	−0.1704 − 0.9854i	−0.1704 + 0.9854i	1	0
0.27	0.3108	3.2176	3.2176	0.1860
0.3	0.0120	83.1471	83.1471	0.7036
0.35	6.9617E − 04	1.4364E + 03	1.4364E + 03	1.1570

Table 1. Floquet analysis of the system (3.1).

$$\eta(0) = 1 \quad \text{and} \quad \eta_{,\tau}(0) = \frac{\mathrm{i}}{\epsilon}, \tag{3.3}$$

which satisfy the governing equation

$$\epsilon^2 \eta_{,\tau\tau} + \eta = 0. \tag{3.4}$$

The above equation, which can be obtained by taking the limit $\tau \to 0$ of (2.21), physically represents propagating deep water interfacial waves inside the two-layered horizontal tank at rest (i.e. non-oscillating).

Figure 3(a) shows that the system undergoes bounded oscillations for $\beta = 0.2$, which cannot be predicted from the normal-mode theory. As already noted in §2.2, systems with $\beta > 0.25$ start becoming unstable when $\tau > \tau_c$. Within the nth period, the system will grow when $2n\pi + \tau_c < \tau < 2(n+1)\pi - \tau_c$, i.e. the interval when $\mathcal{F}(\tau) < 0$ is satisfied. This fact is evident in figure 3(b) which corresponds to $\beta = 0.27$. Furthermore, the plot also reveals the amplification of energy between consecutive periods. Figures 3(c) and 3(d) respectively correspond to $\beta = 0.5$ and $\beta = 0.8$, and reveal a much larger growth rate, as is expected from the trend observed in table 1.

Finally, we compare the growth rate $\sigma_{numerical}$ obtained from the numerical solutions (calculated when $\tau > \tau_c$) with the normal-mode predictions in (2.27):

(i) $\beta = 0.27$: $\sigma_{normal\text{-}mode} = 2.94$ $\sigma_{numerical} = 0.18$ (amplitude envelope growth rate);
(ii) $\beta = 0.5$: $\sigma_{normal\text{-}mode} = 14.14$ $\sigma_{numerical} = 14.12$;
(iii) $\beta = 0.8$: $\sigma_{normal\text{-}mode} = 26.53$ $\sigma_{numerical} = 26.53$.

As evident from the above data and also from figures 3(c) and 3(d), the normal-mode growth rate predictions from (2.27) provide an excellent agreement with the numerical solution, and this agreement improves even further as β increases. Since the normal-mode growth rate exactly matches with that of the classical KH instability, this conclusively proves that the instability is of KH type. However, for the $\beta = 0.27$ (which is a β value slightly greater than the instability condition) case, the normal-mode theory fails to predict the growth rate of the amplitude envelope, as well as the intricate temporal dynamics of the amplitude evolution, which is clear from figure 3(b).

We also emphasise here that β, by definition, is proportional to $\omega^2 = g'k/2$. The growth rate trend reveals the classical 'ultraviolet catastrophe', i.e. shorter waves are more unstable, which is an artefact of the absence of a length scale (i.e. finite thickness of the interface) in the problem.

Finally, we compare our theoretical predictions with the DNS results of Lewin & Caulfield (2022). In this regard, we choose the case 'NM72D', where normal-mode perturbations have been used to seed the flow. Note that the authors use smooth profiles, hence, their parameters need to be suitably adjusted to fit our discontinuous set-up. Their parameters are as follows: $\alpha_f = 7.28° = 0.127$ radians, $\lambda = 14.28$ implying $k = 0.44$,
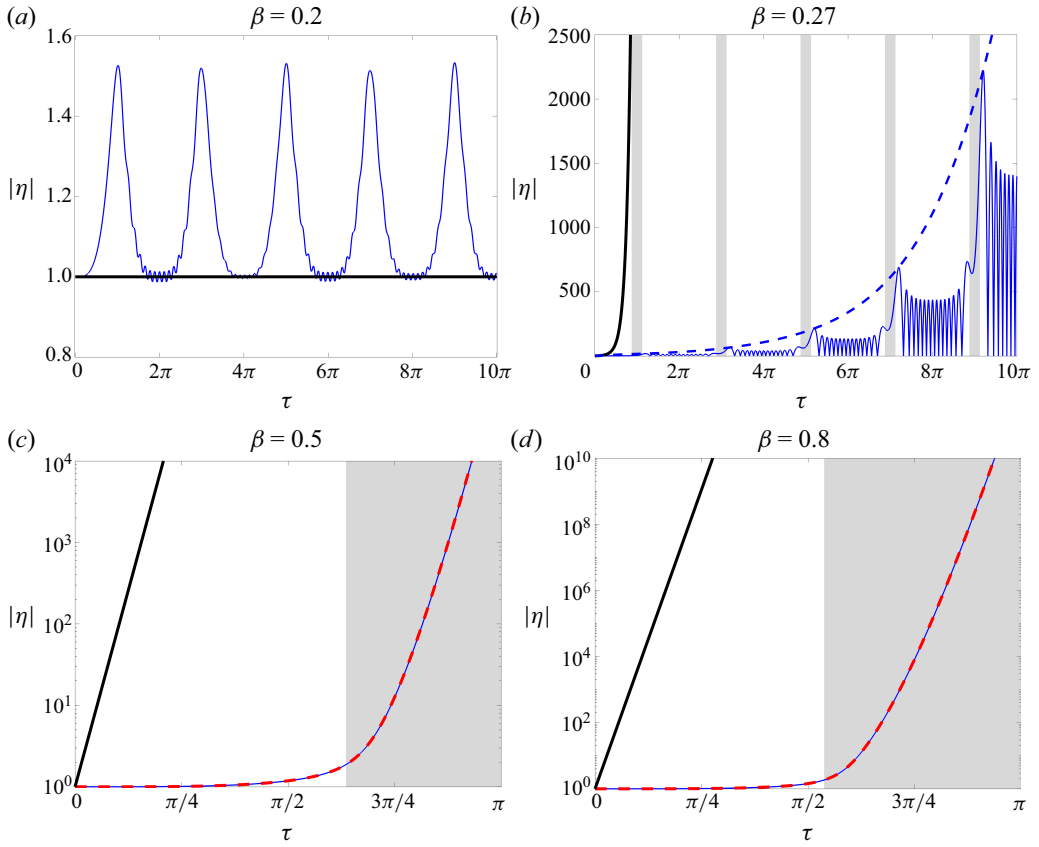
Figure 3. Plots of $|\eta|$ vs τ for different β values. Unstable regions predicted from (2.23) are shaded in grey. Line colours are as follows: black – normal-mode solution (based on steady background flow (2.26)), blue – numerical solution of (2.21) and dashed red – MAF solution (3.21). The dashed-blue line in (*b*) represents the amplitude envelope.

half-shear layer thickness $\delta = 1$ and $\omega_f/N_b = 0.072$, where N_b denotes background buoyancy frequency. Noting that $g' = N_b^2\delta$, we can state ϵ^2 in their variables

$$\epsilon^2 = \frac{\omega_f^2}{\omega^2} = \frac{2}{k\delta}\left(\frac{\omega_f}{N_b}\right)^2 = 0.024. \tag{3.5}$$

This yields

$$\beta = \frac{\alpha_f^2}{\epsilon^2} = 0.67 > \frac{1}{4}, \tag{3.6}$$

and thus the set-up for NM72D satisfies our instability condition (2.22). Indeed, the authors observe KH instability for the case NM72D. Furthermore, the onset of instability predicted from (2.23) is $\tau_c = 0.57\pi$, which excellently matches the corresponding DNS result $\tau_c = 0.54\pi$ (see the Acknowledgement). However, we provide a note of caution that while certain instability characteristics (e.g. τ_c) can have a direct quantitative agreement between discontinuous and smooth profiles, this does not guarantee a correspondence between other instability characteristics. For example, growth rates obtained from discontinuous profiles are unreliable. Moreover, discontinuous profiles cannot predict the

1015 A27-12

band of unstable wavenumbers or the most unstable wavenumber. A proper evaluation of these parameters demands consideration of a finite-thickness shear layer.

3.2. *Asymptotic solution: the modified Airy function method*

Here, we aim to construct an approximate solution to the amplitude evolution. A standard approach in this regard would be to employ the well-known singular perturbation technique – the Wentzel–Kramers–Brillouin (WKB) method (Bender & Orszag 2013). In the WKB method, the asymptotic series in the small parameter ϵ is written as follows:

$$\eta(\tau) \sim \exp\left(\frac{1}{\epsilon}\sum_{n=0}^{\infty}\epsilon^n S_n(\tau)\right), \tag{3.7}$$

where $S_n(\tau)$ denotes the complex phase. Substitution of the above expansion in (2.21) yields the following first-order expressions for η (valid for $0 \leqslant \tau < 2\pi - \tau_c$, i.e. up to the second turning point:

$$\eta(\tau) = \begin{cases} C_1|\mathcal{F}(\tau)|^{-\frac{1}{4}}\,\exp\left(\frac{i}{\epsilon}\int_0^\tau \sqrt{|\mathcal{F}(\tilde{\tau})|}\,\mathrm{d}\tilde{\tau}\right) & \text{for } 0 \leqslant \tau < \tau_c, \\ C_2|\mathcal{F}(\tau)|^{-\frac{1}{4}}\,\exp\left(\frac{1}{\epsilon}\int_{\tau_c}^\tau \sqrt{|\mathcal{F}(\tilde{\tau})|}\,\mathrm{d}\tilde{\tau}\right) & \\ +C_3|\mathcal{F}(\tau)|^{-\frac{1}{4}}\,\exp\left(-\frac{1}{\epsilon}\int_{\tau_c}^\tau \sqrt{|\mathcal{F}(\tilde{\tau})|}\,\mathrm{d}\tilde{\tau}\right) & \text{for } \tau_c < \tau < 2\pi - \tau_c. \end{cases} \tag{3.8}$$

The solution exhibits an oscillatory behaviour when $\tau < \tau_c$ and grows monotonically (the decaying solution would rapidly become insignificant) when $\tau_c < \tau < 2\pi - \tau_c$. Note that C_1 can be straightforwardly determined from (3.3) and yields $C_1 = 1$. To find C_2 and C_3, turning point analysis at $\tau = \tau_c$ is required, which employs Airy functions to match the solutions on the two sides of the turning point. Instead of the standard WKB turning point analysis, we employ the modified Airy function (MAF) method, which can be regarded as an improved variant of WKB. The key aspect of MAF is its recognition of the fact that the Airy functions provide a uniformly valid composite approximation both near and far from a turning point. The MAF method was first introduced by Langer (1935); for a detailed discussion on this technique, also see Ghatak, Gallawa & Goyal (1991), Bender & Orszag (2013) and Wine, Achtymichuk & Marsiglio (2025). Here, we employ MAF to analyse both turning points, and hence obtain a uniformly valid solution for the entire period of 2π. In MAF, the amplitude $\eta(\tau)$ is expressed as

$$\eta(\tau) = \begin{cases} F_1(\tau)Ai\,(\zeta_1(\tau)) + G_1(\tau)Bi\,(\zeta_1(\tau)) & \text{for } 0 \leqslant \tau \leqslant \tau_p, \\ F_2(\tau)Ai\,(\zeta_2(\tau)) + G_2(\tau)Bi\,(\zeta_2(\tau)) & \text{for } \tau_p \leqslant \tau \leqslant 2\pi, \end{cases} \tag{3.9}$$

where $\tau_p = \pi$ is the location of absolute minima of the periodic potential $\mathcal{F}(\tau)$, and $Ai\,(\zeta)$ and $Bi\,(\zeta)$, respectively, the MAFs of the first and second kinds, satisfy

$$Ai_{,\zeta\zeta} - \zeta\,Ai(\zeta) = 0, \quad \text{and} \quad Bi_{,\zeta\zeta} - \zeta\,Bi(\zeta) = 0. \tag{3.10}$$

We will proceed by focusing on one of the terms (say, $F_1(\tau)Ai(\zeta_1(\tau))$) in (3.9), as the other terms follow similar algebra, and they can be treated independently. Substituting $F_1(\tau)Ai(\zeta_1(\tau))$ into the governing equation (2.21) and using the Airy function equations we obtain

$$F_{1,\tau\tau}Ai(\zeta) + 2F_{1,\tau}Ai_{,\zeta_1}\zeta_{1,\tau} + F_1 Ai_{,\zeta_1}\zeta_{1,\tau\tau} + F_1\,Ai(\zeta_1)\big[\epsilon^2\zeta_1(\tau)\zeta_{1,\tau}^2 + \mathcal{F}(\tau)\big] = 0. \tag{3.11}$$

To eliminate the terms in square brackets, $\zeta_1(\tau)$ is chosen to satisfy

$$\epsilon^2 \zeta_1(\tau)[\zeta_{1,\tau}(\tau)]^2 + \mathcal{F}(\tau) = 0, \tag{3.12}$$

which gives

$$\zeta_1(\tau) = \begin{cases} -\left(\dfrac{3}{2\epsilon} \displaystyle\int_\tau^{\tau_c} \sqrt{\mathcal{F}(\tilde{\tau})} \mathrm{d}\tilde{\tau}\right)^{2/3} & \text{for } 0 \leqslant \tau \leqslant \tau_c, \\[4mm] \left(\dfrac{3}{2\epsilon} \displaystyle\int_{\tau_c}^{\tau} \sqrt{-\mathcal{F}(\tilde{\tau})} \mathrm{d}\tilde{\tau}\right)^{2/3} & \text{for } \tau_c \leqslant \tau \leqslant \tau_p. \end{cases} \tag{3.13}$$

Here, $F_1(\tau)$ is obtained by assuming $F_{1,\tau\tau} \approx 0$. Thus, $F_1(\tau)$ satisfies

$$2F_{1,\tau} Ai_{,\zeta_1} \zeta_{,\tau} + F_1 Ai_{,\zeta_1} \zeta_{1,\tau\tau} = 0, \tag{3.14}$$

which leads to

$$F_1(\tau) = \frac{D_1}{\sqrt{\zeta_{1,\tau}(\tau)}}. \tag{3.15}$$

Similarly, $G_1(\tau)$, $F_2(\tau)$, and $G_2(\tau)$ can be expressed as

$$G_1(\tau) = \frac{D_2}{\sqrt{\zeta_{1,\tau}(\tau)}}, \quad F_2(\tau) = \frac{D_3}{\sqrt{\zeta_{2,\tau}(\tau)}} \quad \text{and} \quad G_2(\tau) = \frac{D_4}{\sqrt{\zeta_{2,\tau}(\tau)}}, \tag{3.16}$$

where

$$\zeta_2(\tau) = \begin{cases} \left(\dfrac{3}{2\epsilon} \displaystyle\int_\tau^{2\pi-\tau_c} \sqrt{-\mathcal{F}(\tilde{\tau})} \mathrm{d}\tilde{\tau}\right)^{2/3} & \text{for } \tau_p \leqslant \tau \leqslant 2\pi - \tau_c, \\[4mm] -\left(\dfrac{3}{2\epsilon} \displaystyle\int_{2\pi-\tau_c}^{\tau} \sqrt{\mathcal{F}(\tilde{\tau})} \mathrm{d}\tilde{\tau}\right)^{2/3} & \text{for } 2\pi - \tau_c \leqslant \tau \leqslant 2\pi. \end{cases} \tag{3.17}$$

The arbitrary constants D_1, D_2, D_3 and D_4 will be determined by using the initial conditions (3.3) and the continuity of $\eta(\tau)$ and $\eta_{,\tau}(\tau)$ at $\tau_p = \pi$. The initial conditions (3.3) give

$$\begin{bmatrix} D_1 \\ D_2 \end{bmatrix} = \pi \sqrt{\zeta_{,\tau}(0)} \begin{bmatrix} Bi_{,\tau}(\zeta_1(0)) \\ -Ai_{,\tau}(\zeta_1(0)) \end{bmatrix} - \frac{\pi}{\sqrt{\zeta_{,\tau}(0)}} \left(\frac{\mathrm{i}}{\epsilon} + \frac{\zeta_{,\tau\tau}(0)}{2\zeta_{,\tau}(0)}\right) \begin{bmatrix} Bi(\zeta_1(0)) \\ -Ai(\zeta_1(0)) \end{bmatrix}. \tag{3.18}$$

The continuity of $\eta(\tau)$ and $\eta_{,\tau}(\tau)$ at $\tau_p = \pi$ yields the following system of linear equations with unknowns D_3 and D_4:

$$\begin{bmatrix} A_3(\tau_p) & B_3(\tau_p) \\ A_{3,\tau}(\tau_p) & B_{3,\tau}(\tau_p) \end{bmatrix} \begin{bmatrix} D_3 \\ D_4 \end{bmatrix} = \begin{bmatrix} A_2(\tau_p) & B_2(\tau_p) \\ A_{2,\tau}(\tau_p) & B_{2,\tau}(\tau_p) \end{bmatrix} \begin{bmatrix} D_1 \\ D_2 \end{bmatrix}, \tag{3.19}$$

where

$$A_j(\tau) = \frac{Ai(\zeta_j(\tau))}{\sqrt{\zeta_{j,\tau}(\tau)}} \quad \text{and} \quad B_j(\tau) = \frac{Bi(\zeta_j(\tau))}{\sqrt{\zeta_{j,\tau}(\tau)}} \quad \text{for } j = 2, 3. \tag{3.20}$$

Finally, the MAF solution of (2.21) over one period (and thus capturing both first and second turning points) is given by

$$\eta(\tau) = \begin{cases} (\zeta_{1,\tau}(\tau))^{-1/2} \left[D_1 Ai(\zeta_1(\tau)) + D_2 Bi(\zeta_1(\tau)) \right] & \text{for } 0 \leqslant \tau \leqslant \tau_p, \\[3mm] (\zeta_{2,\tau}(\tau))^{-1/2} \left[D_3 Ai(\zeta_2(\tau)) + D_4 Bi(\zeta_2(\tau)) \right] & \text{for } \tau_p \leqslant \tau \leqslant 2\pi. \end{cases} \tag{3.21}$$
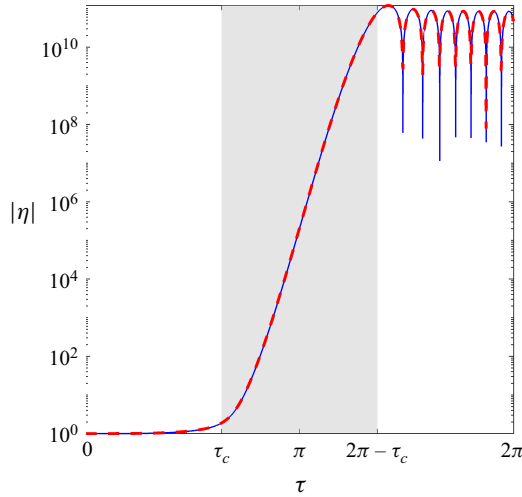
Figure 4. Comparison between numerical solution (blue) and MAF (dashed red) for one period for the case $\beta = 0.5$. The first and second turning points are, respectively, τ_c and $2\pi - \tau_c$; the unstable region predicted from (2.23) is shaded in grey.

Figure 4, which is for the case $\beta = 0.5$, reveals that the MAF solution is nearly indistinguishable from the numerical solution. Unlike figure 3(*c*), figure 4 has been plotted for the entire 2π period and thus includes the behaviour around both turning points. While figure 4 reveals oscillations after the second turning point, the existence of such a behaviour is contentious in reality since, even before the second turning point is reached, the flow is likely to enter the fully nonlinear stages of KH instability, making the linear solution invalid.

4. Numerical simulation: unsteady vortex blob method

Here, we extend the linear interfacial dynamics to the fully nonlinear stages via the vortex blob method, which is a standard numerical technique for capturing the nonlinear evolution of vortex sheets (Baker, Meiron & Orszag 1982; Sohn, Yoon & Hwang 2010; Pozrikidis 2011; Bhardwaj & Guha 2018). The applicability of the vortex blob method to our two-layered oscillating flow problem is fully justified since the two-fluid interface is a vortex sheet, i.e. the tangential component of fluid velocity has a jump discontinuity. In vortex methods, the interface is described as a parametric curve $\boldsymbol{x}(s, t) = (x(s, t), z(s, t))$ with s being the arc-length parameter, and evolves according to

$$\boldsymbol{x}_{,t} = \boldsymbol{q}, \tag{4.1}$$

where $\boldsymbol{q} = (\overline{u}, \overline{w}) = (\boldsymbol{u_1} + \boldsymbol{u_2})/2$ is the arithmetic mean of the velocities above (i.e. $\boldsymbol{u_1} = (u_1, w_1)$) and below (i.e. $\boldsymbol{u_2} = (u_2, w_2)$) the interface. For a domain that is periodic in the along-channel direction x, the velocity $\boldsymbol{q}$ is obtained via the Birkhoff–Rott equation

$$\overline{u} - \mathrm{i}\overline{w} = \frac{\mathrm{i}}{2\lambda} \int_0^\lambda \widetilde{\gamma} \cot\left[\frac{\pi(\chi - \widetilde{\chi})}{\lambda}\right] \mathrm{d}\widetilde{s}, \tag{4.2}$$

where χ is the complex position of the interface: $\chi = x(s, t) + \mathrm{i}z(s, t)$, λ is the wavelength and $\widetilde{\gamma} = \gamma(\widetilde{s}, t)$ denotes the vortex-sheet strength, which is defined as the jump in the

tangential velocities of the two fluids across the interface

$$\gamma = (\boldsymbol{u_1} - \boldsymbol{u_2}) \cdot \hat{\boldsymbol{s}}. \tag{4.3}$$

In order to solve (4.2), the evolution equation for the vortex-sheet strength is needed. To obtain this, first we rewrite (2.2a)–(2.2b) for each layer in a vectorial form

$$\frac{\mathrm{D}\boldsymbol{u_i}}{\mathrm{D}t} = -\frac{1}{\rho_0}\boldsymbol{\nabla} P_i - g\frac{\rho_i}{\rho_0}(\sin \alpha(t)\hat{\boldsymbol{x}} + \cos \alpha(t)\hat{\boldsymbol{z}}) + 2\alpha_{,t}\hat{\boldsymbol{y}} \times \boldsymbol{u_i}, \tag{4.4}$$

where $\boldsymbol{u_i} = (u_i, w_i)$, and $i = 1(2)$ implies upper (lower) layer. Subtracting the equation for $i = 2$ from $i = 1$ and projecting the resultant equation along the tangential direction (by taking an inner product with $\hat{\boldsymbol{s}}$) yields

$$\frac{\mathrm{D}\gamma}{\mathrm{D}t} + \gamma\frac{\partial \boldsymbol{q}}{\partial s} \cdot \hat{\boldsymbol{s}} = g'(\sin \alpha(t)\hat{\boldsymbol{x}} + \cos \alpha(t)\hat{\boldsymbol{z}}) \cdot \hat{\boldsymbol{s}} + [2\alpha_{,t}\hat{\boldsymbol{y}} \times (\boldsymbol{u_1} - \boldsymbol{u_2})]\cdot \hat{\boldsymbol{s}}, \tag{4.5}$$

where $\mathrm{D}/\mathrm{D}t = \partial/\partial t + \boldsymbol{q} \cdot \hat{\boldsymbol{s}} \, \partial/\partial s$. In obtaining (4.5), the continuity of pressure across the interface has been used. Furthermore, using the identities $\hat{\boldsymbol{x}} \cdot \hat{\boldsymbol{s}} = \partial x/\partial s$ and $\hat{\boldsymbol{z}} \cdot \hat{\boldsymbol{s}} = \partial z/\partial s$, we find that the last term on the right-hand side of (4.5), arising from the Coriolis acceleration, vanishes since the interface is a streamline

$$(\hat{\boldsymbol{y}} \times \boldsymbol{u_{1,2}}) \cdot \hat{\boldsymbol{s}} = w_{1,2}\frac{\partial x}{\partial s} - u_{1,2}\frac{\partial z}{\partial s} = 0. \tag{4.6}$$

Previous studies with vortex methods have primarily been restricted to steady background flows (for example, see Sohn *et al.* (2010) and references therein) although the method itself applies to unsteady flows. In our case, the explicit time dependence of the flow clearly manifests on the right-hand side of (4.5) through the angle of oscillation parameter $\alpha(t)$.

For the numerical implementation, we first write (4.2) in a discretised fashion

$$\bar{u}_m = x_{m,t} = \frac{1}{2}\sum_{n=1,n\neq m}^{N} \Gamma_n \frac{\sinh[k(z_m - z_n)]}{\cosh[k(z_m - z_n)] - \cos[k(z_m - z_n)] + \delta^2}, \tag{4.7a}$$

$$\bar{w}_m = z_{m,t} = -\frac{1}{2}\sum_{n=1,n\neq m}^{N} \Gamma_n \frac{\sin[k(x_m - x_n)]}{\cosh[k(z_m - z_n)] - \cos[k(z_m - z_n)] + \delta^2}, \tag{4.7b}$$

where $(\bar{u}_m, \bar{w}_m)$ is the velocity of the mth point vortex (Lagrangian marker) at the location (x_m, z_m), N denotes the total number of point vortices, $k = 2\pi/\lambda$ denotes the wavenumber and δ denotes Kransy's parameter (Krasny 1986) which regularises the otherwise singular kernel in (4.2). The parameter δ can be regarded as a proxy for viscous effects, numerically replacing point vortices with vortex 'blobs', and thereby adding a finite thickness to the otherwise discontinuous shear layer. Finally, Γ_m denotes the circulation of the mth point vortex, which is given as follows:

$$\Gamma_m = \gamma_m \Delta s_m, \tag{4.8}$$

where Δs_m is the arc length about the mth point vortex

$$\Delta s_m = \sqrt{\Delta x_m^2 + \Delta z_m^2}. \tag{4.9}$$

In the above equation, $\Delta x_m = (x_{m+1} - x_{m-1})/2$ and $\Delta z_m = (z_{m+1} - z_{m-1})/2$. Equations (4.7a)–(4.7b) succinctly show that the interaction between the point vortices representing the discretised vortex sheet leads to interface evolution.
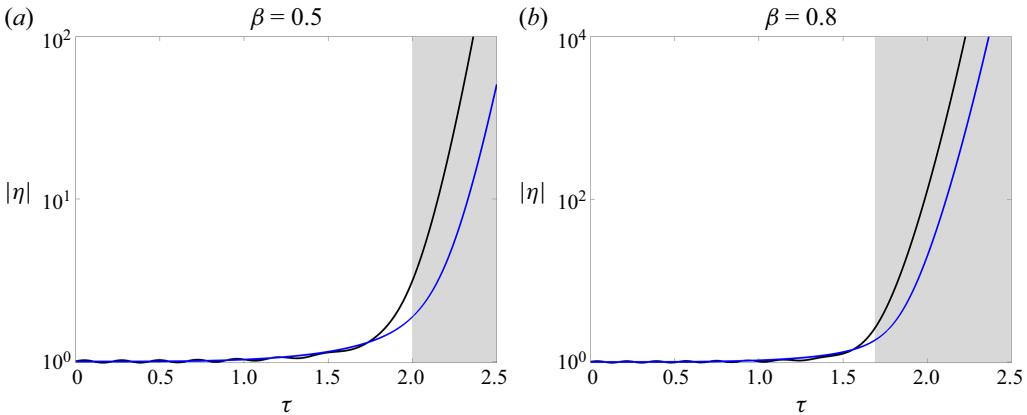
Figure 5. Interface amplitude evolution for different β values. Blue – solution to the linear equation (2.21), black – solution obtained using the vortex method. Unstable region predicted from (2.23) is shaded in grey.

Using (4.8) in (4.5), we obtain the discretised version of the circulation evolution equation

$$\Gamma_{m,t} = \Delta x_m \, g' \sin \alpha(t) + \Delta z_m \, g' \cos \alpha(t). \tag{4.10}$$

Next, we numerically solve (4.7a)–(4.7b) along with (4.10) (where the definition of $\alpha(t)$ is given in (2.8)) using the fourth-order Runge–Kutta time integration scheme. To speed up the computation, we recast the governing equations into the slow-time variable τ. The system is initialised with a short, linear, interfacial gravity wave with the following interfacial displacement, written in a discretised fashion: $z_m = a \cos(k x_m)$, where $x_m = m/N$, $k = 2\pi$ and $a = 10^{-6}$. The initial circulation of the mth point vortex is then given by

$$\Gamma_m(0) = -2\omega z_m \Delta x_m, \tag{4.11}$$

where $\omega = \sqrt{g'k/2} = 0.1772$, and corresponds to $g' = 0.01$. Initially we take $N = 400$. With the progress of time, especially during the highly nonlinear stages, the interface can develop poor resolution in certain locations. To tackle this, we follow the vortex insertion scheme outlined in Sohn *et al.* (2010). In this procedure, a threshold arc length Δs_{thresh} is defined; if the arc length at any location m becomes greater than the threshold, i.e. $\Delta s_m > \Delta s_{thresh}$, then a point vortex is inserted. The x coordinate of the inserted vortex is taken to be the average of the x coordinates of the mth and $(m+1)$th vortices; the same approach is followed for the z coordinate and the circulation. The Kransy parameter δ is chosen accordingly to suppress spurious high wavenumber instabilities.

Figure 5 compares the interface evolution obtained from the linear equation (2.21) with the fully nonlinear solution obtained using the vortex blob method for two different β values. The growth rate and the onset of instability predicted from the vortex method solution agree well with the linear theory.

Figure 6 shows the interface evolution for the case $\beta = 0.8$. The interface rolls up into a KH billow, qualitatively agreeing with the DNS results of Inoue & Smyth (2009) and Lewin & Caulfield (2022). The numerical simulation is run until the billow saturates. Any further late-time dynamics may not be representative of the reality since the vortex method is strictly two-dimensional and hence does not capture the 3-D effects emanating from secondary instabilities, which can crucially alter the dynamical behaviour (Lewin & Caulfield 2022).
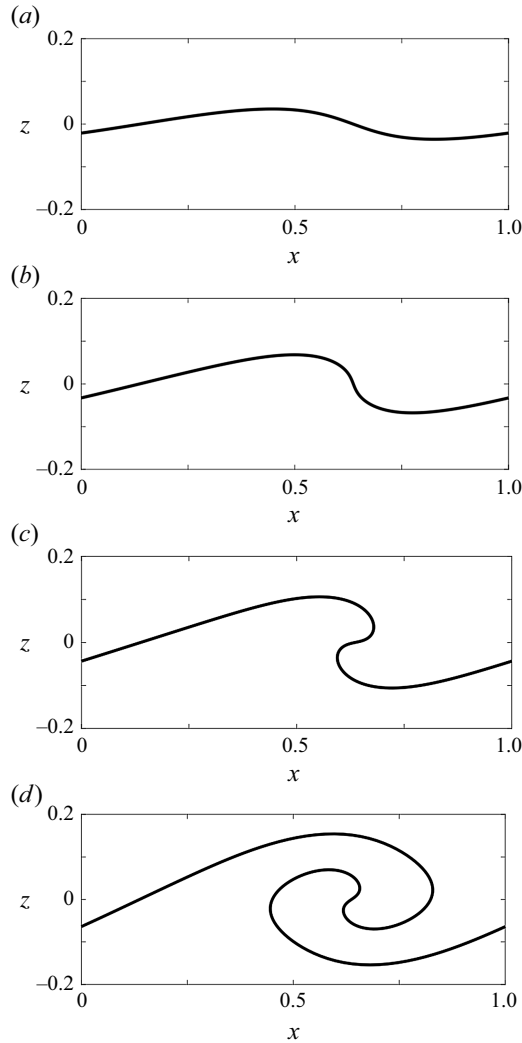
Figure 6. Interface evolution for the case $\beta = 0.8$ for $\tau = 2.285, 2.315, 2.340$ and 2.395.

5. Physical interpretation and case studies

The oscillating tank system is a simplified model for studying instabilities arising in a temporally varying pycnocline in lakes, estuaries and oceans. Pycnocline oscillations are typically generated by wind forcing, or by diurnal and semi-diurnal tides interacting with underwater topography (Sanford *et al.* 1990; Mihanović *et al.* 2009). During the summer months, many shelf seas and lakes reveal a two-layered density stratification (Lemmin *et al.* 2005; Mihanović *et al.* 2009; Guihou *et al.* 2018), providing ideal conditions to compare the flow field induced by low baroclinic mode oscillations of the pycnocline with the oscillating tank system. Below we provide two case studies, one for Lake Geneva and the other for the Chesapeake Bay.

5.1. *Lake Geneva*

We consider the background conditions of the summer of 1950 given in Lemmin *et al.* (2005): $h_1 = 15$ m, $h_2 = 175$ m, $\rho_1 = 998.49$ kg m^{-3} (corresponding to 19 °C) and

$\rho_2 = 1000 \, \text{kg m}^{-3}$ (corresponding to 5.5 °C). The frequency of mode-1 is $\omega_f = 2.14 \times 10^{-5} \, \text{s}^{-1}$ (period of 81.5 h) and corresponds to a Kelvin seiche. The maximum width of the lake is 13.8 km and the maximum difference in thermocline excursions at the two extremities of the lake width (station-3 and station-8) due to mode-1 is ≈ 2 m. Hence, $\tan \alpha_f \approx \alpha_f = 2/13800 = 0.000145$. Since the two layers are of unequal depths, the analysis provided in Appendix A will be applicable. The problem can be simplified since the lower layer is much deeper than the upper layer, which leads to the instability condition $\beta > 1/8$; see (2.24). This yields

$$\beta = \alpha_f^2 \frac{\omega^2}{\omega_f^2} > \frac{1}{8} \Longrightarrow k > \frac{\omega_f^2}{4g'\alpha_f^2} \quad \text{or} \quad \lambda < \frac{8\pi g'\alpha_f^2}{\omega_f^2}. \tag{5.1}$$

For the parameters of Lake Geneva, the above equation would imply that interfacial waves at the pycnocline shorter than $\lambda_{long\text{-}wave\text{-}cut\text{-}off} = 17.03$ m will be rendered unstable. An interfacial wave of wavelength 17 m will start to grow after $\tau_c = \cos^{-1}[1 - (2\beta)^{-1/2}] = 40$ hours (see Appendix A) from initiation of the mode-1 oscillation.

5.2. *Chesapeake Bay*

Here, we consider the background conditions of May/June 1993 of the Chesapeake Bay given in Frizzell-Makowski (1997). In this case, $h_1 = 10$ m, $h_2 = 13$ m, $\rho_1 = 1004 \, \text{kg m}^{-3}$ and $\rho_2 = 1011 \, \text{kg m}^{-3}$. Pycnocline oscillations had a period of 12 h ($\omega_f = 0.00014 \, \text{s}^{-1}$), which was generated by the interaction of semi-diurnal tides with a discontinuity in the bathymetry. Approximately 4 m of vertical displacement over half of the wavelength (0.5×25 km $= 12.5$ km) of the internal tide was observed, yielding $\tan \alpha_f \approx \alpha_f = 4/12500 = 0.00032$. The two layers have unequal depths with $r = h_1/h = 0.435$, yielding the instability condition $\beta > 0.246$. Following the analysis in Appendix A, we obtain

$$\beta = \alpha_f^2 \frac{\omega^2}{\omega_f^2} > 0.246 \Longrightarrow k > \frac{0.492\omega_f^2}{g'\alpha_f^2} \quad \text{or} \quad \lambda < \frac{4.065\pi g'\alpha_f^2}{\omega_f^2}. \tag{5.2}$$

Hence, for the parameters of Chesapeake Bay, interfacial waves at the pycnocline shorter than $\lambda_{long\text{-}wave\text{-}cut\text{-}off} = 4.2$ m will become unstable. This implies that an interfacial wave of wavelength 4 m would start to grow $\tau_c = 5.4$ h (see (A6)) after the inception of the internal tide. However, it is important to note that these values should be taken as a rough estimate since the value of 4.2 m for the longest unstable wavelength is not large enough to disregard the finite-thickness effects of the pycnocline (pycnocline always has a finite thickness, however small).

6. Summary and conclusion

This study uses mathematical and numerical techniques to investigate the generation mechanism and fundamental characteristics of instabilities arising at the density interface in a two-layered oscillating channel flow. The set-up provides a simplified model for studying shear instabilities arising at the density interface due to the time-periodic shear generated by the slow oscillations of the density interface itself. This self-induced shear of the oscillating pycnocline may provide an alternate pathway to turbulence and diapycnal mixing in addition to that obtained via wind-induced shear in the upper ocean or the lake epilimnion.

The equation governing the density interface dynamics, given by (2.21), is a Schrödinger-type equation with a time-periodic potential. The small parameter ϵ, which is

the ratio of the low-frequency pycnocline oscillations (forcing frequency) and the high-frequency short waves (that could be rendered unstable), encapsulates the separation of time scales. This makes (2.21) fundamentally different from the commonly studied time-periodic dynamical systems governed by Mathieu-type equations, which can lead to parametric instabilities. An inverse-Richardson-number-like non-dimensional parameter β determines the necessary and sufficient stability condition of (2.21); for two layers of equal thickness, the flow becomes linearly unstable when $\beta > 1/4$. When the layers have unequal thickness, the stability condition depends on the ratio of layer thicknesses, see Appendix A. Once the instability condition is satisfied, the solution does not start to grow after $\tau = 0+$, but rather tunnels into the unstable state after $\tau = \tau_c$. Using the parameters of a DNS case study in Lewin & Caulfield (2022), we show that our theory correctly predicts the time of onset of instability. Next, we study the interface evolution by numerically solving (2.21) and compare it with the asymptotic solution obtained via the MAF method. We show that MAF provides a uniformly valid composite solution over the entire period (which includes two turning points) and reveals an excellent agreement with the numerical solution. To evaluate the temporal growth rate, we compute the Floquet exponents; furthermore, we also derive the exact normal-mode growth rate obtained for various steady-state-based approximations of the background flow. We observe that the normal-mode theory implemented on a background flow that considers the maximum velocity in each layer (as opposed to the time average over a period) provides a highly accurate growth rate prediction. The normal-mode growth rate is shown to exactly match the classical vortex-sheet KH instability, thereby conclusively proving that the instability is of KH type. Next, we extend the linear analysis of the interface evolution to the fully nonlinear stages via the unsteady vortex blob method. While the standard vortex blob method is commonly implemented for steady background flows, the procedure also applies to time-dependent flows. This needs modification to the circulation evolution equation typically used in vortex methods problems with density stratification. We derive the unsteady circulation evolution (4.10), which captures the explicit time dependence of the flow. The time of the onset of instability as well as the growth rate show good agreement with the predictions from the linear analysis. During the nonlinear stages, the interface rolls up into KH billows, agreeing with the previous DNS studies (Inoue & Smyth 2009; Lewin & Caulfield 2022).

Finally, we provide a physical context to the two-layered oscillating tank model by considering two case studies – Lake Geneva and Chesapeake Bay. Each of these sites reveals pycnocline oscillations, and using the available data, we obtain the stability condition, estimate the time of onset of the shear instabilities as well as the long-wavelength cutoff.

As a closing remark, we reiterate the fact that stability analysis with discontinuous profiles provides spurious growth rates (ultraviolet catastrophe), which necessitates stability analysis of background flows with finite shear layer thickness. The latter is also essential for obtaining the wavenumber corresponding to the maximum growth rate, as well as a short-wavelength cutoff, which cannot be obtained from discontinuous analysis. Despite these limitations, the two-layered configuration studied in this paper provides a foundational basis for the unsteady shear instability mechanism, makes the problem analytically (or semi-analytically) tractable through a simple governing equation, and also provides the necessary and sufficient condition for instability, which leads to key predictions (e.g. the time of onset of instability) that excellently compare with numerical results obtained from smooth profiles.

Appendix A. Derivation of the stability condition for two layers of unequal depths

Let us consider the two layers having different depths, denoted by h_1 and h_2. The background state density distribution is then given by

$$\rho(z) = \begin{cases} \rho_1 & 0 < z < h_1, \\ \rho_2 & -h_2 < z < 0, \end{cases} \tag{A1}$$

where $h_2 = h - h_1$, in which h represents the total channel depth. Following the method outlined in §2.1, the background state velocity profile is given by

$$U(z,t) = \begin{cases} \dfrac{g'h_2}{h} \displaystyle\int_0^t \sin\alpha(\tilde{t})\,d\tilde{t} & 0 < z < h_1, \\ -\dfrac{g'h_1}{h} \displaystyle\int_0^t \sin\alpha(\tilde{t})\,d\tilde{t} & -h_2 < z < 0. \end{cases} \tag{A2}$$

Under the assumption of small oscillations, the background state velocity profile simplifies to

$$U(z,t) = \begin{cases} \dfrac{g'h_2}{h} \dfrac{\alpha_f}{\omega_f}(1 - \cos(\omega_f t)) & 0 < z < h_1, \\ -\dfrac{g'h_1}{h} \dfrac{\alpha_f}{\omega_f}(1 - \cos(\omega_f t)) & -h_2 < z < 0. \end{cases} \tag{A3}$$

Following the procedure in §2.2, infinitesimal perturbations are added to the background state. The waves are assumed to be significantly shorter than the depth of the individual layers, i.e. $kh_1 \gg 1$ and $kh_2 \gg 1$. The evolution equation of the interface $\eta(\tau)$ between the two fluid layers under the Boussinesq approximation is given by

$$\epsilon^2 \eta_{,\tau\tau} + \left[1 - 3\beta\left(r^2 + (1-r)^2\right) + 2\beta\left(r^2 + (1-r)^2\right)\left(2\cos(\tau) - \frac{1}{2}\cos(2\tau)\right)\right.$$
$$\left. + \mathcal{O}\left(\alpha_f^2\right)\right]\eta = 0, \tag{A4}$$

where $r = h_1/h$. All variables and parameters are the same as in §2.2. The necessary and sufficient condition for instability is found to be

$$\beta > \beta_{min} = \frac{1}{8\left[r^2 + (1-r)^2\right]}. \tag{A5}$$

Since $r \in (0,1)$, this implies that $1/8 < \beta_{min} \leqslant 1/4$.

The turning point τ_c, marking the time at which the flow tunnels into the unstable region is given by

$$\tau_c = \cos^{-1}\left(1 - \frac{1}{\sqrt{2\beta\left[r^2 + (1-r)^2\right]}}\right). \tag{A6}$$

The maximum growth rate obtained from the normal-mode analysis is as follows:

$$\sigma_{normal\text{-}mode} = \frac{\sqrt{8\beta\left[r^2 + (1-r)^2\right] - 1}}{\epsilon}. \tag{A7}$$

In a typical oceanographic scenario, the depth of the pycnocline is much smaller than the total depth of the ocean, i.e. $r \ll 1$. In this situation, the instability condition becomes $\beta > 1/8$, the instability will start after $\tau_c = \cos^{-1}[1 - (2\beta)^{-1/2}]$, and the maximum growth rate obtained from the normal-mode method simplifies to $\sigma_{normal\text{-}mode} = \sqrt{8\beta - 1}/\epsilon$.

REFERENCES

ATOUFI, A., ZHU, L., LEFAUVE, A., TAYLOR, J.R., KERSWELL, R.R., DALZIEL, S.B., LAWRENCE, G.A. & LINDEN, P.F. 2023 Stratified inclined duct: two-layer hydraulics and instabilities. *J. Fluid Mech.* **977**, A25.

BAKER, G.R., MEIRON, D.I. & ORSZAG, S.A. 1982 Generalized vortex methods for free-surface flow problems. *J. Fluid Mech.* **123**, 477–501.

BENDER, C.M. & ORSZAG, S.A. 2013 *Advanced Mathematical Methods for Scientists and Engineers I: Asymptotic Methods and Perturbation Theory*. Springer Science & Business Media.

BHARDWAJ, D. & GUHA, A. 2018 Nonlinear modeling of stratified shear instabilities, wave breaking, and wave-topography interactions using vortex method. *Phys. Fluids* **30** (1), 014102.

CARR, M., FRANKLIN, J., KING, S.E., DAVIES, P.A., GRUE, J. & DRITSCHEL, D.G. 2017 The characteristics of billows generated by internal solitary waves. *J. Fluid Mech.* **812**, 541–577.

CAULFIELD, C.P. 2021 Layering, instabilities, and mixing in turbulent stratified flows. *Annu. Rev. Fluid Mech.* **53** (1), 113–145.

CAULFIELD, C.P. & PELTIER, W.R. 2000 The anatomy of the mixing transition in homogeneous and stratified free shear layers. *J. Fluid Mech.* **413**, 1–47.

DAUXOIS, T., *et al.* 2021 Confronting grand challenges in environmental fluid mechanics. *Phys. Rev. Fluids* **6** (2), 020501.

DRAZIN, P.G. & REID, W.H. 2004 *Hydrodynamic Stability*. Cambridge University Press.

FARRELL, B.F. & IOANNOU, P.J. 1996 Generalized stability theory. Part II: Nonautonomous operators. *J. Atmos. Sci.* **53** (14), 2041–2053.

FRIZZELL-MAKOWSKI, L.J. 1997 Temporal variablity of the pycnocline in the mid-Chesapeake Bay.

GHATAK, A., GALLAWA, R. & GOYAL, I. 1991 Modified Airy Function and WKB Solutions to the Wave Equation. Monograph (NIST MN). National Institute of Standards and Technology.

GUHA, A. & RAHMANI, M. 2019 Predicting vortex merging and ensuing turbulence characteristics in shear layers from initial conditions. *J. Fluid Mech.* **878**, R4.

GUIHOU, K., POLTON, J., HARLE, J., WAKELIN, S., O'DEA, E. & HOLT, J. 2018 Kilometric scale modeling of the North West European Shelf Seas: exploring the spatial and temporal variability of internal tides. *J. Geophys. Res. Oceans* **123** (1), 688–707.

VAN HAREN, H. & GOSTIAUX, L. 2010 A deep-ocean Kelvin–Helmholtz billow train. *Geophys. Res. Lett.* **37** (3), L03605.

INOUE, R. & SMYTH, W.D. 2009 Efficiency of mixing forced by unsteady shear flow. *J. Phys. Oceanogr.* **39** (5), 1150–1166.

KELLY, R.E. 1965 The stability of an unsteady Kelvin–Helmholtz flow. *J. Fluid Mech.* **22** (3), 547–560.

KOVACIC, I., RAND, R. & MOHAMED SAH, S. 2018 Mathieu's equation and its generalizations: overview of stability charts and their features. *Appl. Mech. Rev.* **70** (2), 020802.

KRASNY, R. 1986 Desingularization of periodic vortex sheet roll-up. *J. Comput. Phys.* **65** (2), 292–313.

LANGER, R.E. 1935 On the asymptotic solutions of ordinary differential equations, with reference to the Stokes' phenomenon about a singular point. *Trans. Am. Math. Soc.* **37** (3), 397–416.

LEMMIN, U., MORTIMER, C.H. & BÄUERLE, E. 2005 Internal seiche dynamics in Lake Geneva. *Limnol. Oceanogr.* **50** (1), 207–216.

LEWIN, S.F. & CAULFIELD, C.P. 2022 Stratified turbulent mixing in oscillating shear flows. *J. Fluid Mech.* **944**, R3.

MACKINNON, J.A. & GREGG, M.C. 2005 Spring mixing: turbulence and internal waves during restratification on the New England shelf. *J. Phys. Oceanogr.* **35** (12), 2425–2443.

MacKinnon, J.A., *et al.* 2017 Climate process team on internal wave–driven ocean mixing. *Bull. Am. Meteorol. Soc.* **98** (11), 2429–2454.

Mashayek, A., Caulfield, C.P. & Alford, M.H. 2021 Goldilocks mixing in oceanic shear-induced turbulent overturns. *J. Fluid Mech.* **928**, A1.

Mashayek, A. & Peltier, W.R. 2012 The 'zoo' of secondary instabilities precursory to stratified shear flow transition. Part 1 Shear aligned convection, pairing, and braid instabilities. *J. Fluid Mech.* **708**, 5–44.

Mihanović, H., Orlić, M. & Pasarić, Z. 2009 Diurnal thermocline oscillations driven by tidal flow around an island in the Middle Adriatic. *J. Mar. Syst.* **78**, S157–S168.

Onuki, Y., Joubaud, S. & Dauxois, T. 2021 Simulating turbulent mixing caused by local instability of internal gravity waves. *J. Fluid Mech.* **915**, A77.

Pozrikidis, C. 2011 *Introduction to Theoretical and Computational Fluid Dynamics*. Oxford University Press.

Rahmani, M., Lawrence, G.A. & Seymour, B.R. 2014 The effect of Reynolds number on mixing in Kelvin–Helmholtz billows. *J. Fluid Mech.* **759**, 612–641.

Richards, D. 2002 *Advanced Mathematical Methods with Maple*. Cambridge University Press.

Sanford, L.P., Sellner, K.G. & Breitburg, D.L. 1990 Covariability of dissolved oxygen with physical processes in the summertime Chesapeake Bay. *J. Mar. Res.* **48** (3), 567–590.

Smyth, W.D. & Moum, J.N. 2012 Ocean Mixing by Kelvin–Helmholtz Instability. *Oceanography* **25** (2), 140–149.

Sohn, S.-I., Yoon, D. & Hwang, W. 2010 Long-time simulations of the Kelvin–Helmholtz instability using an adaptive vortex method. *Phys. Rev. E* **82** (4), 046711.

Sutherland, B.R. 2010 *Internal Gravity Waves*. Cambridge University Press.

Thorpe, S.A. 1969 Experiments on the instability of stratified shear flows: immiscible fluids. *J. Fluid Mech.* **39** (1), 25–48.

Wine, N., Achtymichuk, J. & Marsiglio, F. 2025 The modified airy function approximation applied to the double-well potential. *AIP Adv.* **15** (3), 3.

Wunsch, C. & Ferrari, R. 2004 Vertical mixing, energy, and the general circulation of the oceans. *Annu. Rev. Fluid Mech.* **36** (1), 281–314.

Zhu, L., Atoufi, A., Lefauve, A., Kerswell, R.R. & Linden, P.F. 2024 Long-wave instabilities of sloping stratified exchange flows. *J. Fluid Mech.* **983**, A12.